

## HYDRODYNAMIC SIMULATIONS OF H $\alpha$ EMISSION IN ALGOL-TYPE BINARIES

MERCEDES T. RICHARDS<sup>1</sup> AND MARK A. RATLIFF<sup>2</sup>

Department of Astronomy, University of Virginia, P.O. Box 3818, Charlottesville, VA 22903-0818

Received 1996 July 8; accepted 1997 September 2

### ABSTRACT

Two-dimensional hydrodynamic simulations of mass transfer in short-period Algol-type binaries were performed using the numerical code Virginia Hydrodynamics 1. This code uses the piecewise parabolic method with a Lagrangian remap. Our version of the code also accounts for radiative cooling and collisional ionization and excitation processes. The purpose of performing the simulations was to study the H $\alpha$  emission from circumstellar gas in the Algols. Using observational evidence from the literature to constrain the gas stream properties, hydrodynamic maps of the H $\alpha$  emissivity in the two systems  $\beta$  Per ( $P = 2.87$  days) and TT Hya ( $P = 6.95$  days) were made in both Cartesian and velocity coordinates from the simulation data. The velocity maps were then compared to Doppler tomograms constructed from observed H $\alpha$  line emission in these systems. Since the tomograms cannot be directly transformed to maps of emission in spatial coordinates, the simulated Cartesian maps enabled us to interpret the dynamical processes that produce the features observed in the Doppler tomograms. We find that the simulations produce asymmetric accretion structures with many features similar to those found in the Doppler tomograms of Algol systems.

*Subject headings:* accretion, accretion disks — binaries: eclipsing — circumstellar matter — hydrodynamics — stars: imaging — stars: individual (U Coronae Borealis, TT Hydrae,  $\beta$  Persei, U Sagittae, V711 Tauri)

### 1. INTRODUCTION

Algol-type binaries are composed of a B- to A-type main sequence star, the “primary,” and a fainter, evolved F- to K-type giant or subgiant, the “secondary.” As a result of evolution, the secondary star expands until its photosphere extends beyond its Roche lobe. During Roche lobe overflow, gas flows through the first Lagrangian point ( $L_1$  point) and forms a gas stream (also known as mass transfer stream, tidal stream, or matter stream) inside the Roche lobe of the more massive primary star (Fig. 1). The type of trajectory the gas stream follows as it falls toward the primary is largely dependent upon the orbital separation and radii of the two stars. For instance, if the radius of the primary is relatively small compared to the orbital separation, the gas stream will be deflected by the Coriolis force into an orbit about the primary. The gas stream in this type of system may then feed into a stable accretion disk surrounding the star. However, if the radius of the primary is large compared to the orbital separation, the Coriolis force is not large enough to deflect the gas stream away from an impact trajectory with the photosphere of the primary star. We are primarily concerned with these “direct impact” systems in this work.

When undergoing mass transfer via Roche lobe overflow, the Algol binaries that have periods longer than about 6 days display double-peaked H $\alpha$  line profiles indicative of classical accretion disks, while systems with periods less than 6 days exhibit variable disk structure (Peters 1989; Kaitchuck, Honeycutt, & Schlegel 1985). The semi-analytical ballistic calculations of Lubow & Shu (1975) indicate that direct star-stream impact is likely to occur as a result of Roche lobe overflow in the latter of these two groups. For this reason, Peters (1989) and Kaitchuck et al. (1985) suggested that the variability of the accretion struc-

tures in these short-period systems ( $P_{\text{orb}} < 6$  days) is due to the nature of the star-stream impact. In this scenario, the stream burrows into the atmosphere and photosphere of the primary until it reaches a point at which the ambient pressure in the star is equal to the ram pressure of the gas stream. At that point a shock forms, and the gas stream is reflected. Much of the gas stream, along with some of the material that it has churned up in the photosphere of the star, then exits the photosphere and atmosphere of the primary. Since this material has insufficient kinetic energy to escape the gravitational attraction of the primary, it enters an eccentric orbit around the star and gives rise to an unstable, asymmetric, turbulent accretion structure. This structure was originally called a “transient accretion disk” (Kaitchuck et al. 1985). However, since it does not have the Keplerian velocity field ( $v \propto r^{-1/2}$ ) characteristic of the stable accretion disks found in compact binaries, it was renamed the “accretion annulus” to avoid any confusion with a classical accretion disk (Richards, Jones, & Swain 1996).

The accretion structures in these latter systems have been determined from studies of the H $\alpha$  line profiles at orbital positions (phases) around the binary (e.g., Richards 1992; Vesper & Honeycutt 1993). In the case of  $\beta$  Per, the data suggested the presence of a transient accretion annulus, although evidence for the presence of a gas stream was ambiguous owing to projection effects (Richards 1992). In particular, these projection effects made it difficult to conclude whether most of the observed H $\alpha$  emission came from a gas stream or from a localized region located just above the photosphere of the primary in the direction facing the secondary. Since then, the technique of Doppler tomography has been used by Richards and collaborators (e.g., Richards, Albright, & Bowles 1995; Richards, Jones, & Swain 1996; Albright & Richards 1996) to investigate the emission structures in short-period Algol binaries. This technique provides a reconstructed two-dimensional image of the emission sources in velocity coordinates based on the

<sup>1</sup> mrichards@virginia.edu.

<sup>2</sup> mar4g@virginia.edu.

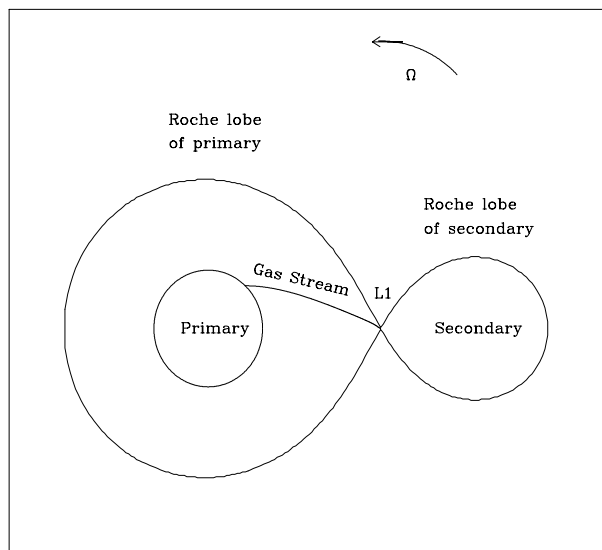


FIG. 1.—Roche geometry of a close, semidetached Algol binary

Doppler shifts of the emission-line profiles around the orbit (Marsh & Horne 1988; Russ 1992; Robinson, Marsh, & Smak 1993).

Several sources of H $\alpha$  emission have now been identified in the Doppler tomograms of the direct-impact systems  $\beta$  Per, RS Vul, U Sge, U CrB, SW Cyg, and TT Hya (Richards et al. 1995, 1996). These systems display the presence of a gas stream (in U CrB and U Sge), an accretion annulus (in the short-period systems  $\beta$  Per, RS Vul, U Sge, U CrB), an accretion disk (in the long-period systems SW Cyg and TT Hya), and possible chromospheric emission from the secondary (in RS Vul). The distribution of these emission sources in the tomogram is also time dependent (Albright & Richards 1996). In particular, one of the tomograms of U CrB shows that the gas stream follows the predicted free-fall path in velocity space. Since there are multiple asymmetric and time-dependent emission sources in these binaries, there is no simple, one-to-one mapping between the emission in velocity space and that in Cartesian space. So, the exact Cartesian locations of the emitting regions are not readily inferred from the velocities of the emission features. This realization led the authors toward an alternative approach to interpret the Doppler tomograms.

Hydrodynamic calculations were first used by Blondin, Richards, & Malinkowski (1995; hereafter BRM) to simulate the structures formed as a result of direct-impact accretion in Algol binaries. They performed two-dimensional hydrodynamic simulations of the Algol system ( $\beta$  Per) and investigated the accretion flows and their dependence on various parameters such as the density and velocity of the gas stream. Those simulations produced an extended accretion annulus whose structure was dependent upon the radiative cooling rate of the circumstellar gas around the primary. In particular, when the stream density was high ( $n_s \sim 10^9 \text{ cm}^{-3}$ ), the accreted gas was confined to a thin ring near the surface of the primary because of efficient cooling. However, when the stream density was low ( $n_s \sim 10^8 \text{ cm}^{-3}$ ), the gas expanded to fill most of the Roche lobe of the primary because inefficient cooling permitted the gas to heat and expand. These simulations illustrated the properties of the flow quite effectively in the Cartesian coordinate frame, but they did not display the velocity structure of the

gas flows and did not include the emission-line characteristics. As a result, the simulations of BRM could not be directly compared with the reconstructed Doppler images derived from spectroscopic observations of the Algol binary.

In this work, we specifically address the need for hydrodynamic simulations that could be directly compared with observational results. In particular, we performed two-dimensional simulations of two interacting binaries: the short-period Algol,  $\beta$  Per ( $P = 2.87$  days), and the long-period system, TT Hya ( $P = 6.95$  days). The former system was chosen to illustrate the case of direct-impact accretion in which an accretion annulus should form, and the latter binary was chosen to illustrate the case in which a classical accretion disk should form. We have also extended the previous work initiated by BRM by producing maps of the H $\alpha$  emissivity of the circumstellar gas in both Cartesian and velocity coordinates. The velocity maps produced from the simulations were compared with the Doppler tomograms of Algols obtained by Richards et al. (1995, 1996) in order to correlate the emission features in the Doppler maps with corresponding structures in Cartesian space. The velocity maps of TT Hya were also compared with the Doppler tomograms of cataclysmic variables (Kaitchuck et al. 1994) that also have accretion disks.

In the next section, we describe the numerical code and model used to perform the hydrodynamic simulations. Section 3 describes the results of the simulations, and concluding remarks are given in § 4. The preliminary results of this work were given in Ratliff (1996) and Ratliff & Richards (1995).

## 2. THE NUMERICAL MODEL

The two-dimensional simulations in this work were performed with the numerical code, Virginia Hydrodynamics 1 (VH-1), written by the Numerical Astrophysics Group at the Virginia Institute for Theoretical Astrophysics (Blondin 1993). VH-1 uses the scheme known as PPMLR, which is a version of the Piecewise Parabolic Method (PPM) of Colella & Woodward (1984) implemented in Lagrangian coordinates coupled with a remap onto fixed Eulerian coordinates after each time step.

Several assumptions were made in order to apply the VH-1 code to the study of direct-impact accretion. We assumed that the gas flow was initiated at the  $L_1$  point and was acted on only by gravitational forces in the rotating reference frame. A cylindrical coordinate grid was set up with its origin at the center of mass of the mass-gaining star (the primary). The inner boundary of the grid coincided with the photosphere of the primary star, and the outer boundary was designed to include the entire Roche lobe of the mass-losing star (the secondary). We assumed a partially reflecting boundary at the photosphere of the primary to partially compensate for accretion onto the primary star.

The numerical model discussed here is along the lines described by BRM and was designed, at this stage, to illustrate the first-order characteristics of the gas flows in direct-impact binaries. The BRM paper addressed several issues related to this astrophysical problem, and we will only summarize those discussions here. The assumption of a partially reflecting boundary condition at the surface of the primary is justified by the relatively small scale height of the stellar atmosphere on the primary star ( $\sim 10^8 \text{ cm}$ ) compared to the radius of the gas stream ( $\sim 10^{10} \text{ cm}$ ) and the fact that the

stream does not penetrate deep into the photosphere ( $\sim 10^6$  cm; Richards 1992), where the hydrogen lines are formed. The circumstellar gas was assumed to be equivalent to an optically thin, cosmic abundance plasma in ionization equilibrium. This fluid was evolved using an adiabatic equation of state with  $\gamma = 5/3$  and includes optically thin radiative cooling via the method of operator splitting. Note that while the opacity of the circumstellar material could affect the observed spectrum, it is insufficient to influence the total cooling rate. The stellar radiation field was also assumed to keep the circumstellar gas ionized and warm, and a minimum temperature of 8,000 K was imposed during the evolution of the hydrodynamic flow.

The main improvement of the current models over those of BRM is the calculation of the  $H\alpha$  emissivity in addition to the density, pressure, velocity, and temperature structure of the flow. The emission is used as a tracer of the velocity field because the results would be compared directly with the Doppler tomograms derived from the observations. This assumption is accurate to first order, especially since it is difficult to distinguish between the various influences on the line broadening when interpreting the observed spectra. However, Doppler broadening dominates the line shape, while turbulent and other line-broadening mechanisms are less important. In future work, we will extend the model to include radiative transfer effects and calculate synthetic integrated line profiles.

Next, we will discuss the PPMLR code, the computational grid, boundary conditions, calculation of  $H\alpha$  emissivity, the influence of radiative cooling and ionization on the gas flows, and the influence of instabilities on the results.

### 2.1. The PPMLR Code

The Lagrangian coordinate system readily facilitates the interpretation of the fluid equations, since fluid elements are followed as if they were individual particles comoving with the fluid. The equations of fluid dynamics in Lagrangian mass coordinates are

$$\frac{\partial V}{\partial t} - \frac{\partial(r^\alpha u)}{\partial m} = 0, \quad \frac{\partial u}{\partial t} + r^\alpha \frac{\partial P}{\partial m} = f, \quad \frac{\partial E}{\partial t} + \frac{\partial(r^\alpha u P)}{\partial m} = u f, \quad (1)$$

when written in conservative form with no source terms. In these equations,  $V = 1/\rho$  is the specific volume,  $\rho$  is the density,  $u$  is the velocity,  $E$  is the total energy per unit volume,  $f$  is the sum of all body forces,  $P$  is the gas pressure,  $r$  is the Eulerian radial coordinate, and  $m$  is the Lagrangian mass coordinate. The parameter  $\alpha$  is equal to 0, 1, or 2, corresponding to planar, cylindrical, or spherical symmetry, respectively. In addition, the Lagrangian mass coordinate is defined by the relation

$$m(r, t) = \int_{r_0}^r r^\alpha \rho(r, t) dr.$$

These are the equations that are used to evolve the fluid variables. Although it is easy to utilize the Lagrangian mass coordinate, it is not intuitively clear how to interpret the conservation equations spatially. The transformation of these equations from Lagrangian to Eulerian coordinates is not explicitly described by Colella & Woodward (1984) or Blondin (1993). However, it can be shown that these equations reduce to the more familiar Eulerian conservation equations given the following transformations of the differ-

ential operators from Lagrangian to Eulerian coordinates,

$$\frac{\partial}{\partial m} \rightarrow \frac{1}{r^\alpha \rho} \frac{\partial}{\partial r} \quad \text{and} \quad \frac{\partial}{\partial t} \rightarrow \frac{\partial}{\partial t} + u \frac{\partial}{\partial r} = \frac{D}{Dt}.$$

These transformations show that the simple time derivative,  $\partial/\partial t$ , in the Lagrangian mass coordinate is equivalent to the more complex material derivative,  $D/Dt$ , in Eulerian coordinates. Thus, advection of conserved quantities in Eulerian coordinates is equivalent to a simple time derivative in mass coordinates. It is this quality that makes it easy to use the mass coordinate.

The conservation equations (eq. [1]) are used to evolve the zone-centered, volume-averaged values of  $V$ ,  $u$ , and  $E$ , given knowledge of the gradient across the grid zone of the quantities  $r^\alpha u$ ,  $P$ , and  $r^\alpha u P$ , respectively. Numerically, the gradient of a quantity across a zone is approximated by the finite difference of that quantity evaluated at the zone boundaries, divided by the difference in the coordinate position of the zone boundaries. In addition, since this gradient will be treated as a constant over the present time step when used to evolve a fluid variable, it is most appropriate to use a value that is time-averaged over the present time step. The evaluation of these time-averaged quantities at the zone boundaries is the main computational task of PPM. However, once these quantities have been evaluated, the conservation equations can, in principle, be finite-differenced as

$$V_j^{n+1} = V_j^n + \frac{\Delta t}{\Delta m} [(\bar{r}_{j+1/2})^\alpha \bar{u}_{j+1/2} - (\bar{r}_{j-1/2})^\alpha \bar{u}_{j-1/2}], \quad (2a)$$

$$u_j^{n+1} = u_j^n - \frac{\Delta t}{\Delta m} (\bar{r}_j)^\alpha [\bar{P}_{j+1/2} - \bar{P}_{j-1/2}] + \frac{\Delta t}{2} (f_j^{n+1} + f_j^n), \quad (2b)$$

$$E_j^{n+1} = E_j^n - \frac{\Delta t}{\Delta m} [(\bar{r}_{j+1/2})^\alpha \bar{u}_{j+1/2} \bar{P}_{j+1/2} - (\bar{r}_{j-1/2})^\alpha \bar{u}_{j-1/2} \bar{P}_{j-1/2}] + \frac{\Delta t}{2} (u_j^{n+1} f_j^{n+1} + u_j^n f_j^n), \quad (2c)$$

where the superscript  $n$  or  $n+1$  refers to the time step at which the particular quantity is evaluated, while the subscript  $j$ ,  $j - \frac{1}{2}$ , or  $j + \frac{1}{2}$  refers to whether the quantity is evaluated at zone center, the left zone boundary, or the right zone boundary, respectively. Also, the line over some of the variables on the right-hand side of these equations indicates the value of these variables averaged over the present time step. The time-averaged value of the body forces in these equations is found by evaluating these forces at the beginning and end of the time step and averaging the two values. This procedure requires knowledge of the forces at the next time step. Depending on the form of the forces, this information is not always available. In this case, some reasonable approximation to the value of the body forces at the next time step is needed, or another independent equation must be invoked to evolve the forces to the next time step.

Given a complete knowledge of all body forces, the evaluation of the time-averaged fluid variables at the zone boundaries is the key to evolving the conservation equations. The method by which any scheme finds these values is its defining characteristic. The PPM uses the Godunov method (Godunov 1959) of solving a separate Riemann

problem at each zone boundary to find the time-averaged value of the pressure and velocity of the fluid at that boundary. These values can then be used in the finite-differenced conservation equations (eqs. [2a]–[2c]) to evolve the fluid variables.

The Riemann problem that the Godunov method employs is a situation where two physically identical gases (i.e., same average particle mass and same adiabatic index,  $\gamma$ ) having different density, pressure, and velocities are separated by a thin membrane that is subsequently allowed to burst. When the membrane bursts, allowing the gases to interact, a shock wave or rarefaction wave will propagate through each gas on either side of the membrane, bringing the gases to a state of uniform pressure and velocity. The values of the uniform pressure and velocity are then used as the time-averaged pressure and velocity evaluated at the zone boundary. For simplicity and ease of application, the method tacitly assumes that rarefaction waves propagate as discontinuities in exactly the same way that shock waves propagate (Colella & Woodward 1984). Therefore, both the wave running to the right and the wave running to the left of the zone boundary must satisfy the Rankine-Hugoniot jump conditions:

$$\frac{\bar{P} - P_R}{W_R} + (\bar{u} - u_R) = 0, \quad (3a)$$

$$V_R = \frac{\gamma P_R}{\rho_R} \left[ 1 + \frac{\gamma + 1}{2\gamma} \left( \frac{\bar{P}}{P_R} - 1 \right) \right], \quad (3b)$$

and

$$\frac{\bar{P} - P_L}{W_L} + (\bar{u} - u_L) = 0, \quad (4a)$$

$$V_L = \frac{\gamma P_L}{\rho_L} \left[ 1 + \frac{\gamma + 1}{2\gamma} \left( \frac{\bar{P}}{P_L} - 1 \right) \right], \quad (4b)$$

where  $P_{R(L)}$  and  $u_{R(L)}$  are the pressure and velocity, respectively, of the fluid to the right (left) of the zone boundary before the membrane has burst,  $V_{R(L)}$  is the speed of the shock or rarefaction wave that travels through the right (left) zone after the membrane has burst, and  $\bar{P}$  and  $\bar{u}$  are the uniform pressure and velocity of the fluid that has been overtaken by a wave. Given the values of  $u_R$ ,  $u_L$ ,  $P_R$ , and  $P_L$ , there results four equations in the four unknowns  $\bar{P}$ ,  $\bar{u}$ ,  $V_R$ , and  $V_L$ . These equations can then be solved for the quantities we seek, namely,  $\bar{P}$  and  $\bar{u}$ .

The final problem, then, is to find values for the input states,  $P_{R(L)}$  and  $u_{R(L)}$ , to be used in the jump equations (3) and (4). The simplest method would be to use the zone-averaged values of  $P$  and  $u$  in the zones to the left and right of the zone boundary. This is exactly the method that the first-order Godunov scheme employs. However, all of the fluid in a grid zone adjacent to the boundary cannot possibly have an effect on the boundary in a given time step because of the finite propagation speed of information. The fluid from which a sound wave can propagate to the zone boundary within the present time step is the only fluid that can influence the Riemann problem. For this reason, the PPM attempts to resolve the variation of a fluid variable across a zone by interpolating for that variable using a parabolic profile. Such an interpolation, performed for a particular fluid variable in a particular zone, is constructed at each time step by using the zone-averaged values of that

variable in the four nearest neighboring zones of the zone over which the interpolation is taking place. This interpolation must have the quality that its value averaged over an entire zone is exactly equal to the zone-averaged value in that zone, while it also attempts to capture the way in which the variable changes from zone to zone. In some sense, this interpolation has the effect of increasing the resolution of the simulation beyond the grid spacing. Finally, using the knowledge of how the variable changes through the zone, the value of the variable to be used as input into the Riemann problem is taken to be the average of that quantity in the region between the zone boundary and the distance to which a sound wave can propagate away from the boundary in the present time step. This region is called the “domain of influence” because material outside this region will not be able to affect the zone boundary within the present time step. The average on either side of the zone boundary is obtained simply by integrating the interpolated parabolic profile over the corresponding domain of influence and then dividing by the volume contained in that domain. Use of such an interpolation function within a grid zone, therefore, allows for the calculation of the input states appropriate for the fluid that has influence on the Riemann problem.

The interpolation parabolae were chosen carefully to avoid generating spurious structure in the zone-averaged quantities on length scales smaller than the grid spacing. In regions where the zone average of a variable changes significantly between two neighboring zones, the interpolation can introduce extrema not seen in the zone-averaged data. The extrema appear as inflections or waves in the interpolations. These features are suppressed by requiring that the interpolation functions increase or decrease monotonically as a function of coordinate position within each zone. In addition, the interpolation functions are forced to take on a constant value in a zone where an extremum in the zone-averaged values occurs. Finally, in zones not containing an extremum in the zone-averaged values, the value given by the interpolation parabola anywhere in the zone is forced to lie within the range spanned by the zone-averaged values of the two neighboring zones. These conditions tend to flatten sharp bumps in the interpolations. This is essentially the same as damping wavelike structure on length scales smaller than the zone spacing. These procedures define the monotonicity conditions placed on the interpolation parabolae and inhibit the formation of any wavelike structure on a length scale smaller than that resolved by the grid spacing.

The basic scheme of the code can now be summarized. First, at each time step, the average value of the fluid variables on each side of zone boundaries is found by averaging interpolation parabolae over a suitable domain of influence subject to certain conditions for continuity and monotonicity on these parabolae. These average values are then used as input states to the Riemann problem in order to calculate the time-averaged value of  $u$  and  $P$  at the zone boundaries. The PPM finally uses these values to evaluate the gradients in the conservation equations in order to evolve the fluid variables in Lagrangian coordinates. However, the PPMLR extends this scheme one step further by mapping the results from Lagrangian coordinates back onto fixed Eulerian coordinates. It is this step that allows the scheme to be implemented in two spatial dimensions. However, before any of these calculations can be performed, the initial conditions and boundary conditions of the simu-

lation must be determined. These conditions are unique to the particular numerical problem under consideration.

## 2.2. The Computational Grid and Boundary Conditions

The computational grid was designed to surround the primary star and to include as much of the binary system as possible. A cylindrical coordinate system with 200–300 azimuthal zones and 150 radial zones was constructed and centered on the mass-gaining primary star. The grid was designed to rotate about the center of mass of the binary system with a period equal to the orbital period of the binary. Since the most active part of the flow was expected to lie near the surface of the mass-gaining star, the radial dimension of each successive grid zone was reduced by a decrement of 1% in the direction approaching the primary star, thereby increasing the spatial resolution near the surface of the star. Finally, the inner radial boundary of the grid was set at the surface of the primary star, while the outer radial boundary was set to ensure that the secondary star was entirely contained within the grid.

The VH-1 code artificially extends the range of the fluid beyond each boundary to circumvent discontinuities in the fluid. This is accomplished by adding “ghost zones” to the edges of the grid. After each time step, the parameters of the fluid in the ghost zones were reset according to predetermined criteria. These criteria depended on an a priori knowledge of the fluid properties at the boundary. Consequently, the fluid in the ghost zones was not evolved from time step to time step as was done for the fluid contained on the grid. Since we expect the transition between the fluid properties on both sides of the outer boundary around the binary (grid to ghost zones) to be smooth, we implemented a “zero gradient” boundary condition. This algorithm fixed the values of density, pressure, and velocity of the fluid in the ghost zones to be exactly equal to their values at the edge of the grid just within the boundary. An additional constraint was placed on the fluid velocity to prevent fluid from flowing out of the ghost zones onto the grid at speeds greater than the local sound speed. This condition allowed fluid to flow freely onto and off the grid depending solely upon the behavior of the fluid adjacent to the grid boundary. However, we expect a sharp transition across the inner boundary once the fluid interacts with the denser stellar surface. The boundary condition used in this case depends sensitively on the expected behavior of the fluid at the photosphere.

The treatment of the inner boundary condition is based on results of Richards (1992) for the case of  $\beta$  Per. The analysis is summarized here and also applied to the case of TT Hya. In  $\beta$  Per, the gas stream strikes the surface of the primary and penetrates below the surface to a point where the gas pressure in the photosphere,  $P_{\text{phot}}$ , is equal to the ram pressure of the gas stream,  $P_{\text{ram}} = \rho_s v_s^2$ , where  $\rho_s$  is the density and  $v_s$  is the velocity of the gas stream at impact. Assuming that the stream velocity at impact is equal to the free-fall velocity, the ram pressure can be written in terms of the mass transfer rate,  $\dot{M}$ , and the sound speed in the gas stream,  $c_s$ , as

$$P_{\text{ram}} = \frac{\dot{M}}{c_s^2} \left( \frac{G^3 M_1^3}{32 R_1^7} \right)^{1/2},$$

(Ulrich & Burger 1976) where  $M_1$  and  $R_1$  are, respectively, the mass and radius of the primary star and  $G$  is the gravita-

tional constant. In the case of  $\beta$  Per, Richards (1992) compared the ram pressure corresponding to the range of mass transfer rates ( $10^{-11} M_\odot \text{ yr}^{-1} < \dot{M} < 10^{-9} M_\odot \text{ yr}^{-1}$ ) with stellar atmosphere models to show that the stream penetrates to, at most, a distance of  $\sim 10^{-5} R_1$  below the photosphere of the primary.

In the case of TT Hya, the stream is expected to make an even more oblique trajectory than in  $\beta$  Per, and there would only be an initial grazing impact with the stellar surface. In both cases, a perfectly reflecting boundary condition would be adequate, with the exception that material injected onto the grid through the  $L_1$  point would continue to pile up on the grid. So, we have used a “partially reflecting” boundary condition to partially compensate for accretion onto the star. In this case, the gas velocity was set to zero in the first few radial zones while instituting the “zero gradient” condition in the adjacent ghost zones. This allowed the gas stream to shock and reflect from the surface of the primary while also allowing some of the circumpriary gas to accrete onto the central star.

Since the entire secondary star was included on the grid in our simulations (and not in BRM), we developed a special treatment to permit gas to flow out of the secondary through the  $L_1$  point only and restricted gas from flowing out in any other direction. To restrict the flow, the pressure and density in grid zones lying interior to the surface of the secondary were reset to constant floor values after each time step. These floor values were small compared to those found in the rest of the simulation. However, to initiate Roche lobe overflow, gas was set to flow out of the secondary by resetting the pressure, density, and velocity to fixed amounts in a few (e.g., six) zones near the  $L_1$  point. These fixed amounts represent the properties of the gas stream in the vicinity of the  $L_1$  point and are dependent on the particular system under study. These quantities will be revisited when the properties of the two binaries are discussed.

Finally, since the azimuthal coordinate is periodic, one edge of the grid was simply matched to the other in the azimuthal direction. This “periodic” boundary condition was implemented by setting the properties of the fluid in the ghost zones on one edge of the grid identical to those at the opposite edge of the grid.

## 2.3. Calculation of H $\alpha$ Emissivity

The H $\alpha$  emissivity of the gas in each grid zone was calculated in order to compare the results of the simulations to observed tomograms calculated from H $\alpha$  spectra. Given the temperature and density of the gas, the H $\alpha$  emissivity of the gas,  $j_{\text{H}\alpha}$ , was calculated using the formulas for H $\beta$  emission found in Ferland (1980),

$$\frac{4\pi j_{\text{H}\beta}}{N_p N_e} = \begin{cases} 2.53 \times 10^{-22} T_e^{-0.833}, & \text{for } T_e \leq 2.6 \times 10^4 \\ 1.12 \times 10^{-20} T_e^{-1.2}, & \text{for } T_e > 2.6 \times 10^4 \end{cases} \text{ ergs}^{-1} \text{ cm}^3,$$

combined with an assumed Balmer decrement,  $j_{\text{H}\alpha}/j_{\text{H}\beta} = 2.9$ . Note that the observations cannot be used to refine any calculated estimates of the Balmer decrement because of the uncertainty in the observational estimates (Richards 1993). The wide range of temperatures accounted for by these formulas was useful given that the temperature in our simulations could vary from the minimum of 8000 K up to millions of degrees in regions where the gas stream strikes the primary. Although the value of the Balmer decrement is

expected to vary by 10% over this range in temperatures, we decided not to take this effect into account for the sake of simplicity. In our analysis of the simulation results, we primarily examine comparative values of emissivity from region to region. Since we are interested in regional variations in emissivity values by factors of 10–100, then the error incurred by our assumption of a constant Balmer decrement is acceptable. A plot of the resulting H $\alpha$  emissivity,  $j_{\text{H}\alpha}$ , versus temperature,  $T$ , appears in Figure 2.

#### 2.4. Radiative Cooling and Ionization

Radiative cooling in an accretion shock has often been described as a power law in density,  $\rho$ , and temperature,  $T$ :  $j \propto \rho^a T^b$  (Wu, Chanmugan, & Shaviv 1994). Earlier cooling functions such as those of Cox & Daltabuit (1971) considered optically thin collisional ionization models. However, more recent functions calculated by Sutherland & Dopita (1993) provide modeling for low and high temperatures, including both collisional shock and photoionization models. In calculating loss rates, they include a wide range of processes such as fine structure, intersystem, and forbidden emission, as well as resonance transitions and full continuum calculations on an ion-by-ion basis. Calculations for up to 16 atoms (H to Ni) and all stages of ionization for  $\log T = 5$ –8.5 are included. These Sutherland & Dopita (1993) models provide an incremental advance over earlier models, which we expect will not have a significant impact on our simulations. Like BRM, we used the Cox & Daltabuit (1971) cooling function to account for radiative energy losses from the circumstellar gas because the cooling function of Sutherland & Dopita (1993) was not widely accepted at the time. The Sutherland & Dopita models will be used in future simulations.

The Cox & Daltabuit (1971) cooling function gives the radiative energy losses due mainly to permitted lines of carbon and oxygen in an optically thin cosmic abundance plasma in ionization equilibrium. The differential equation for the loss of internal energy in the gas is  $de/dt = -q(N_e, N_p, T)$ , where  $e$  is the internal energy of the gas,  $q$  is the analytic function describing the cooling curve,  $N_e$  and  $N_p$  are the free electron and proton number densities, respec-

tively, and  $T$  is the gas temperature. This differential equation was solved numerically at the end of each time step by using the backward Eulerian scheme along with the secant method for solving the resulting implicit equation (Press et al. 1988).

The effect of ionizing radiation from the primary star was also considered. Using data from Kurucz (1991) models and particle densities typical of those found in the circumstellar gas in the simulations ( $\sim 10^6 \text{ cm}^{-3}$ ), we found the Strömgren radius of the primary to be significant compared to the binary separation in both systems. In  $\beta$  Per, the calculated Strömgren radius was several times the orbital separation, while in TT Hya the radius was approximately equal to the distance between the two stars. For this reason, we assumed that the gas was completely ionized throughout the simulation and implemented a minimum temperature of 8000 K during the evolution of the hydrodynamic flow.

#### 2.5. Influence of Instabilities

Since partially reflecting boundary conditions were used on the primary star, evolution of the flow would produce accretion structures that would not be able to adequately accrete onto the star. As a result, the simulation was evolved for two orbital cycles only, but it was clear that the essential features of the flow had been observed more than once during this time interval. These results are not merely artifacts of instabilities in the flow, but it is important to describe two influential instabilities here.

The Rayleigh-Taylor and Kelvin-Helmholtz instabilities have different effects on the flow and operate on different timescales. The Rayleigh-Taylor instability is a buoyancy-driven instability that forces fluid interchange in situations where the density gradient is negative (i.e., when the heavier fluid is on top of lighter fluid). This instability acts only in the presence of gravitational forces. In the case of the mass transfer in Algols, this instability would lead to mixing in the impact zone where the higher density gas stream makes contact with the lower density atmosphere or photosphere of the primary star. The instability would be restricted to a small region of the flow. Unlike the Rayleigh-Taylor instability, the Kelvin-Helmholtz instability can occur even in the absence of gravitational forces. This latter instability is driven by shearing motions between two regions that have different flow velocities. It would create vortices in the flow to erase the velocity discontinuity, and the mixing would continue in the boundary layer until stability is achieved in the flow (Birkhoff 1962; Tritton 1988; Shore 1992). In our simulations, the K-H instability would act over the region of the flow around the star between the stellar surface and the circumstellar gas. It is this instability that has the larger influence on the properties of the circumstellar gas in the case of  $\beta$  Per where the gas stream makes direct contact with the stellar surface. It is less important in the case of wider binaries, like TT Hya, where the gas stream makes only an initial grazing impact with the star. In both binaries, the size of the boundary layer was small relative to the linear dimensions of the flow. Moreover, there was no evidence to suggest that the instabilities dominate the flow on timescales less than  $\sim 2P_{\text{orb}}$ . Since the basic structure and trajectory of the gas stream are predicted independently by the semianalytical ballistic calculations of Lubow & Shu (1975), then the stream flow up to the impact zone cannot be an artifact of instabilities. Even in the presence of the K-H instability, it is this gas stream that will dominate the

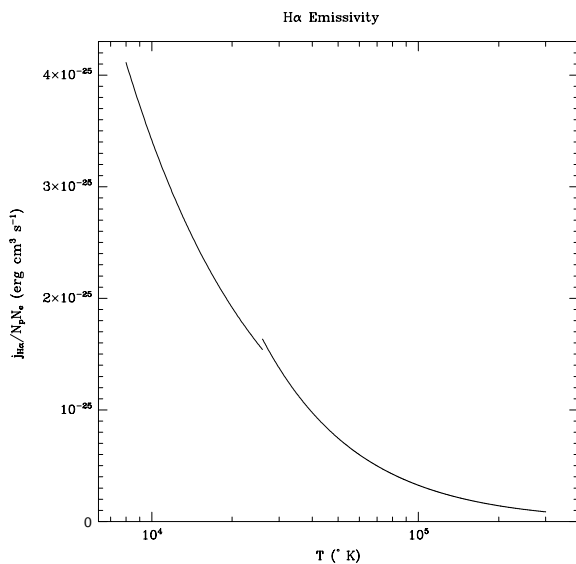


FIG. 2.—Temperature dependence of H $\alpha$  emissivity calculated using the formulas in Ferland (1980) with an assumed Balmer decrement of 2.9.

flow of gas around the primary star. This circumstellar flow is unlikely to smooth out in time because a small disturbance in the flow around the star could deflect the incoming gas stream slightly which, in turn, would generate larger disturbances that would orbit the star and further influence the incoming stream. Moreover, these disturbances are unlikely to disappear within one or two orbits in the absence of a source of strong dissipation (like rapid cooling), so the system is unlikely to ever quiet down. For these reasons, it is appropriate to consider the simulations obtained within two orbital cycles as representative of the flow.

The remaining parameters in the simulations were dependent upon the characteristics of the particular system being studied. The observed characteristics of each binary and the results of the simulations will be discussed in turn in the sections that follow.

### 3. SIMULATION RESULTS

In this section we present the results of the numerical simulations of two Algol-type binary systems,  $\beta$  Per and TT Hya. The properties of the gas flow in these binaries were investigated primarily to study the H $\alpha$  emissivity simultaneously in Cartesian ( $x$ ,  $y$ ) coordinates and velocity ( $v_x$ ,  $v_y$ ) coordinates. The evolution of the temperature and normalized density of the gas flows were also examined in Cartesian coordinates for the  $\beta$  Per simulations. The temperature maps were made to locate the regions where ultraviolet or X-ray emission would be expected. In general, the density simulations were reminiscent of the H $\alpha$  emissivity maps.

Starting at the  $L_1$  point, the simulations were followed for two orbital cycles ( $2P_{\text{orb}}$ ) and at three densities characteristic of the initial gas stream:  $10^8$ ,  $10^9$ , and  $10^{10} \text{ cm}^{-3}$ . Integrated H $\alpha$  emissivity velocity maps were made at these three densities to facilitate comparison with the observed Doppler tomograms of the binaries. These integrated maps were made by adding the H $\alpha$  emissivity from 50 snapshots of the simulation in velocity coordinates during the time interval  $1.0P_{\text{orb}} < t < 2.0P_{\text{orb}}$ . The resulting integrated image represents the system beyond the stage where an accretion annulus completely surrounds the primary star ( $t \approx 1.0P_{\text{orb}}$ ). Since the Doppler tomograms are constructed from many H $\alpha$  observations obtained over multiple orbital periods of the system, the integrated image is more appropriate for comparison with observed tomograms than images constructed at discrete times in the simulation.

Both TT Hya and  $\beta$  Per are Algol-type interacting binaries, but there are some important differences between their physical properties (see Table 1). First, the orbital period of TT Hya ( $P_{\text{orb}} = 6.95$  days) is significantly longer than that of  $\beta$  Per ( $P_{\text{orb}} = 2.87$  days) so that TT Hya is the more widely separated binary. In addition, the ratio of the radius of the primary ( $R_p$ ) to the orbital separation ( $a$ ) in  $\beta$  Per,  $R_p/a = 0.206$ , is much greater than that in TT Hya,  $R_p/a = 0.092$ . These characteristics cause the gas flow to behave differently in these two systems. In particular, the free-falling gas stream in  $\beta$  Per will directly impact and reflect from the surface of the primary star, whereas in TT Hya the star-stream interaction will not be so severe, allowing the stream to form a more stable accretion disk as it orbits the primary.

A preliminary analysis of the expected gas stream trajectory reveals the basic similarities and differences between the two systems. The initial trajectory of the gas stream is

TABLE 1  
SYSTEM PARAMETERS FOR  $\beta$  PER AND TT HYA

Star Parameter	$\beta$ Per <sup>a</sup>	TT Hya <sup>b</sup>
Primary:		
Mass, $M_1$ ( $M_\odot$ ) .....	3.7	2.6
Radius, $R_1$ ( $R_\odot$ ) .....	2.9	2.1
Temperature, $T_1$ (K) .....	13000	10000
Secondary:		
Mass, $M_2$ ( $M_\odot$ ) .....	0.8	0.7
Radius, $R_2$ ( $R_\odot$ ) .....	3.5	5.6
Temperature, $T_2$ (K) .....	4500	5200
Binary:		
Binary separation, $a$ (cm) .....	$9.76 \times 10^{11}$	$1.59 \times 10^{12}$
Orbital period, $P_{\text{orb}}$ (days) .....	2.87	6.95

<sup>a</sup> Richards 1993.

<sup>b</sup> Giuricin, Mardirossian, & Mezzetti (1983).

quite similar in both binaries. Material leaves the  $L_1$  point at relatively low speed as it begins to fall toward the primary star. As it leaves, the net gravitational force and the fictitious Coriolis and centrifugal forces are quite small compared to what they will become at later times. As the gas stream velocity increases owing to gravitational infall, the Coriolis force increases. While the gravitational force attempts to pull the stream straight toward the center of the primary, the Coriolis force pushes the stream in the direction of orbital rotation (Fig. 3). For some time, the components of these two forces perpendicular to the stream nearly cancel each other. The stream therefore travels in nearly a straight line while being accelerated along its length. However, as the stream approaches sufficiently close to the primary, the gravitational force begins to completely dominate. Whether or not the stream will actually impact the primary depends on the stream velocity and the distance between the stream and the surface of the primary star when the gravitational force begins to dominate. The two systems studied below were chosen to demonstrate both the case where the stream strikes the primary directly and where the stream makes merely a grazing impact with the surface of

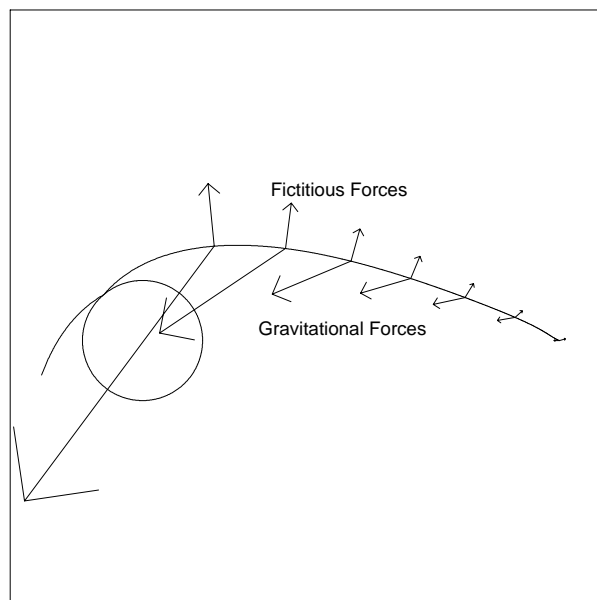


FIG. 3.—Gravitational and fictitious Coriolis and centrifugal forces acting on the gas stream at various locations along the free-fall trajectory of the stream.

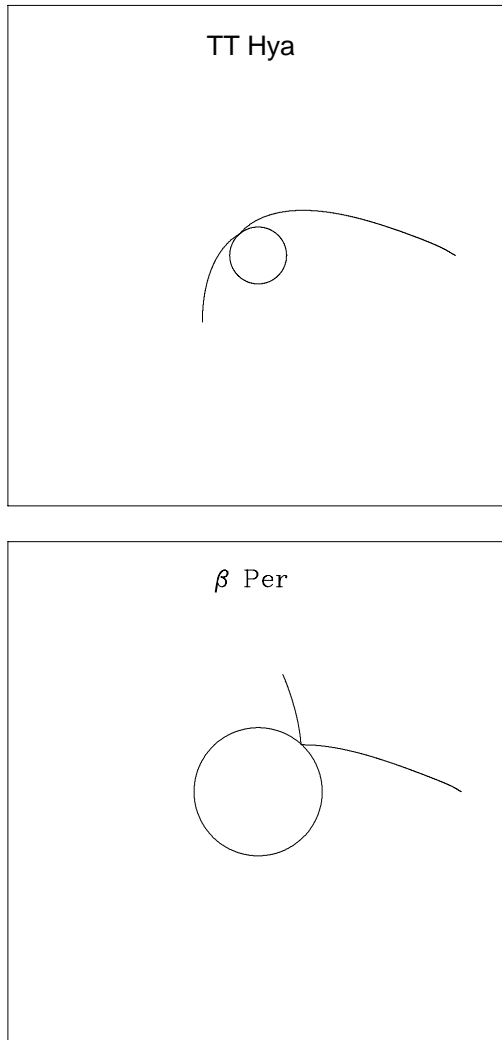


FIG. 4.—Free-fall trajectory of a particle released from the  $L_1$  point as it falls toward the primary in  $\beta$  Per (bottom) and TT Hya (top). The TT Hya figure illustrates a glancing impact of the gas stream, whereas the  $\beta$  Per figure illustrates a gas stream that makes direct impact with the primary star.

the primary (Fig. 4). The differences in the gas flow in these binaries is expected to be caused by the differing location and angle of stream impact on the primary star in each system.

### 3.1. $\beta$ Per

#### 3.1.1. Parameters Specific to the Binary

Algol ( $\beta$  Per) is the prototype of the Algol-type binaries. The system contains a B8 main-sequence star called the primary and a K2 subgiant companion called the secondary. The system also contains an F1 V tertiary companion in a long-period ( $P_{\text{long}} = 1.86$  yr) orbit about the binary (Richards 1993). Since the tertiary is very distant from the binary, this star does not influence the mass transfer process and was therefore not included in our simulations. The physical parameters of the  $\beta$  Per binary system are given in Table 1. The only remaining parameters of interest for the simulation are the gas stream properties, namely its size, density, and velocity at which it leaves the  $L_1$  point.

Since the photospheric temperatures of the secondary star are quite low, we took the temperature of the gas

stream at the  $L_1$  point to be  $T_s = 8,000$  K, which was the minimum temperature allowed in the simulation. The analytic calculations of Lubow & Shu (1975) show that the diameter of the gas stream at  $L_1$  is expected to be on the order of  $c_s/\Omega$ , where  $c_s = (kT_s/m)^{1/2}$  is the sound speed in the gas stream,  $\Omega = 2\pi/P_{\text{orb}}$  is the angular velocity of the binary,  $k$  is the Boltzmann constant, and  $m$  is the mean molecular weight of the gas composing the stream. Assuming that the gas is composed of completely ionized hydrogen (i.e.,  $m = 8.35 \times 10^{-25}$  g), this analysis shows the stream diameter to be  $(c_s/\Omega) \approx 3.5 \times 10^{10}$  cm in the neighborhood of  $L_1$ . In order to capture some of the dynamics that take place within the stream due to its interaction with circumstellar material, we set the stream to be three zones wide. This required the grid to be divided into 300 azimuthal zones, while in the radial direction the grid was divided into 150 zones.

The initial velocity of the gas stream at  $L_1$  was also determined from the analytic calculations of Lubow & Shu (1975). They showed that the stream should reach sonic velocity within a close neighborhood of the  $L_1$  point. Therefore, the stream was set to leave  $L_1$  at the initial sound speed,  $c_s \sim 10$  km s $^{-1}$ .

The stream density was chosen through consideration of both observational evidence and the hydrodynamic simulations previously performed by BRM. Using the size of the emitting region in  $\beta$  Per derived from H $\alpha$  observations, Richards (1992) found the electron density in the circumstellar gas to be  $N_e > 10^{10}$  cm $^{-3}$ . However, because of the uncertainty involved in the assumed volume of the emitting region, this density is only an order-of-magnitude estimate. Moreover, it is uncertain how this circumstellar density compares to the density in the gas stream. From a theoretical standpoint, BRM argue that radiative cooling causes the gas flow to become essentially isothermal for stream densities much greater than  $6 \times 10^8$  cm $^{-3}$ . In this isothermal case, hydrodynamic simulations produce a gas stream with almost no accompanying accretion annulus. Consequently, since an extended accretion annulus was found around the primary in  $\beta$  Per ( $r_d = 1.85R_1$ ; Richards 1992), this suggests that the density in the gas stream should be near  $6 \times 10^8$  cm $^{-3}$ . To examine the effects of a range of densities, we performed three simulations for this system with initial stream densities of  $n_s = 10^8$ ,  $10^9$ , and  $10^{10}$  cm $^{-3}$ , respectively.

#### 3.1.2. Simulations in Cartesian and Velocity Dimensions

In this section, we describe the kinematics and hydrodynamics of the stream, the interaction between the stream and the primary star, and the asymmetric accretion structure that is subsequently formed in the simulations. In order to facilitate the discussion and analysis of the flow in Cartesian and velocity coordinates, we define coordinate directions  $x$  and  $y$  (Fig. 5, *left-hand frame*) in the binary system. The  $x$ -direction is defined to always point from the primary to the secondary star along the line of centers. The  $y$ -direction is defined to be orthogonal to the  $x$ -direction and to point in the direction of the secondary's orbital motion about the primary. The velocity components,  $v_x$  and  $v_y$ , are then defined according to these directions.

Images of the emission in velocity coordinates were constructed by using the gas velocities calculated in the simulations and the orbital parameters of the binary system (Ratliff 1996). These velocity images contain two reference



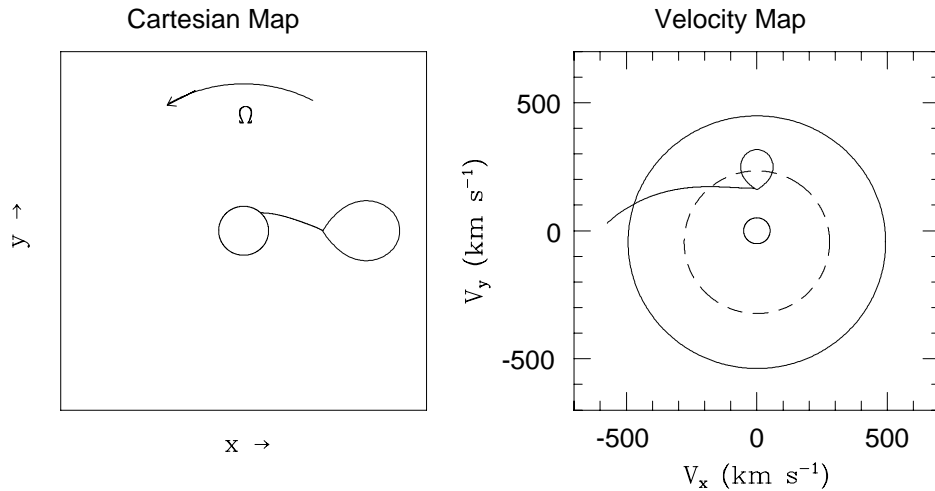


FIG. 5.—Cartesian coordinate system defined for the binary system is shown (*left-hand frame*) along with the velocity coordinate system (*right-hand frame*). The synchronously rotating surfaces of the primary and the secondary as well as the gas stream are shown in their corresponding locations in both figures. The dashed and solid reference circles on the velocity map are consistent with those defined by Richards et al. (1996).

circles (Fig. 5, *right-hand frame*) defined in the same way as by Richards et al. (1996). The solid outer circle represents the size of the Keplerian orbital velocity at the surface of the primary, whereas the inner circle represents the size of the Keplerian velocity at the  $L_1$  point. A classical Keplerian accretion disk would therefore be expected to be between these two reference circles.

Figure 6 shows the evolution of the gas flow for the  $\beta$  Per simulation with initial stream density set at  $n_s = 10^9 \text{ cm}^{-3}$ . The three images represent “snapshots” of the  $\text{H}\alpha$  emissivity in Cartesian and velocity coordinates taken at different times during the simulation. The top row of images shows the state of the system as the stream has become fully extended between the two stars and is about to strike the primary. These two images describe the behavior of the stream as it free falls toward the primary star. During this initial free fall, the stream experiences no significant interaction with other circumstellar material. The Cartesian image (Fig. 6, *top left-hand panel*) shows that the stream narrows as it leaves the  $L_1$  point and falls toward the mass-gaining star. This decrease in stream width is due primarily to the fact that the flow lines converge as the gas falls into the converging gravitational potential of the primary star. As it falls, the gas is accelerated, causing the density in the stream to decrease.

By the time the stream reaches the primary star ( $t = 9.7 \text{ hr} = 0.14P_{\text{orb}}$ ), the gas in the stream has attained a velocity of  $500 \text{ km s}^{-1}$ , and its density has decreased by about a factor of 100 to  $n_s = 10^7 \text{ cm}^{-3}$ . The velocity image corresponding to the time just before impact (Fig. 6, *top right-hand panel*) shows that the gas stream has become fully extended, almost horizontal in the negative  $v_x$  coordinate to the left of the secondary star. In contrast to the narrowing stream in the Cartesian image (Fig. 6, *top left-hand panel*), the stream in the velocity image appears to spread as it falls, becoming wider at higher negative  $v_x$  velocities. This spreading is due to velocity shear present across the width of the stream. Shortly after the time shown in these images, the stream strikes the primary at  $47^\circ$  from the line of centers as measured from the center of the primary. The gas reflected by the impact has velocities close to  $500 \text{ km s}^{-1}$  and temperatures of a few million degrees. This reflected gas is

much too hot to contribute significant amounts of  $\text{H}\alpha$  emission. However, as this gas continues to travel outward from the primary star, it eventually forms a shock with the ambient orbiting material, becoming dense and, later, cool enough to again contribute considerable  $\text{H}\alpha$  emission.

The two images in the middle row of Figure 6 show the time at which gas reflected by the primary has orbited once and then interacts with the gas stream itself ( $t = 34.7 \text{ hr} = 0.5P_{\text{orb}}$ ). The effects of this interaction are most pronounced near the surface of the primary star, where the stream is least dense due to acceleration during free fall. The Cartesian image (Fig. 6, *middle left-hand panel*) shows that the once-orbited material has enough momentum and pressure to momentarily push the gas stream away from its direct-impact trajectory with the primary. This opens a small channel between the primary and the stream through which the orbiting gas can continue its motion. At this time, the part of the stream closest to the primary has a wavy appearance owing to Rayleigh-Taylor instability, as it is pushed by the less dense, once-orbited gas. The velocity image (Fig. 6, *middle right-hand panel*) shows the prominent gas stream with patchy emission from filamentary disk material. These filaments are caused by the instability of the cooling mechanism (i.e., the densest regions are most efficient at cooling and so become denser). The strongest emission feature from the disk material is located below the stream at negative  $v_y$  velocities.

The bottom row of images (Fig. 6) shows the state of the system after two orbital periods have elapsed ( $t = 68.9 \text{ hr} = 2.0P_{\text{orb}}$ ). At this time the primary is completely surrounded by accreted gas (Fig. 6, *lower left-hand panel*). The gas forms an asymmetric accretion annulus containing the filamentary structures seen in the previous images. In the velocity image (Fig. 6, *lower right-hand panel*), the emission is still dominated by the gas stream. However, the emission from the disk material has become more uniformly distributed about the position of the primary star. Ignoring emission from the stream, the brightest emission is located just below the stream in the velocity image. Continuing from that position in the counterclockwise direction about the center of the image, the circumstellar emission becomes continually fainter, forming smaller disconnected patches of

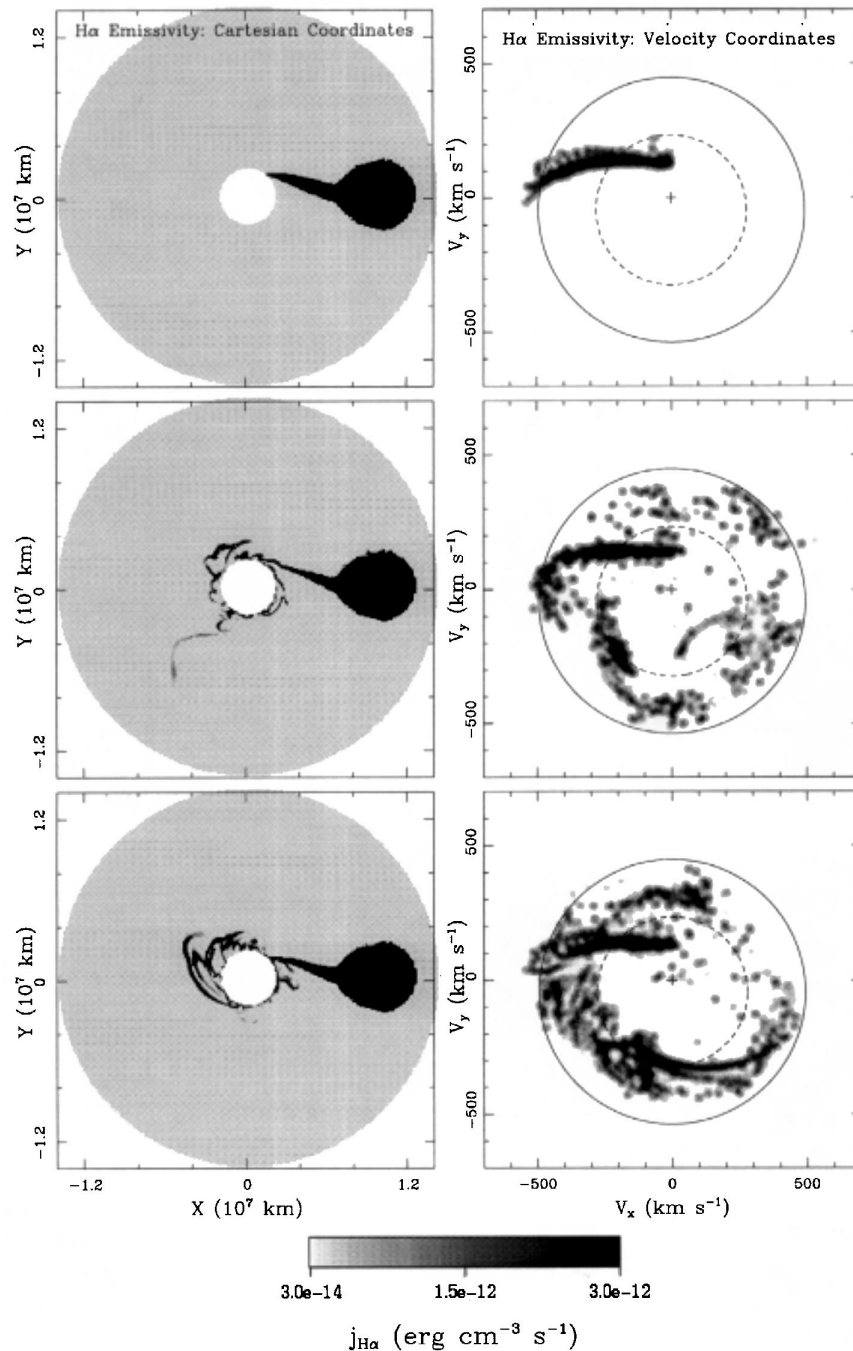


FIG. 6.—Evolution of the H $\alpha$  emissivity of the gas flow in  $\beta$  Per. From top to bottom, the images show the system after time  $t = 9.7$  hr  $= 0.14P_{\text{orb}}$ ,  $t = 34.7$  hr  $= 0.5P_{\text{orb}}$ , and  $t = 68.9$  hr  $= 2.0P_{\text{orb}}$ , respectively. The location of H $\alpha$  emission in Cartesian coordinates is shown on the left, while the distribution of H $\alpha$  emission in velocity coordinates is shown on the right.

emission. This trend is explained by two processes in addition to the Kelvin-Helmholtz instability. In orbiting the primary, some of the gas close to the star is accreted (flows through the inner radial boundary), while the more extended hot gas diffuses, causing its density to decrease. Both of these processes cause a noticeable decrease in the amount of H $\alpha$  emission measured as gas travels in its orbit about the primary. Thus, we see that emission from gas at negative  $v_y$  velocities (where the gas has not been in orbit for a long time) is generally more intense and spread over a larger area than emission from gas in the upper part of the image at positive  $v_y$  velocities.

Figure 7 shows that the density and temperature structure in the three different simulations varies considerably. This result is to be expected considering the nature of the cooling function. The low-density simulation (Fig. 7, *top row*) shows a smoother distribution of gas than does the higher density simulation (Fig. 7, *middle row*), which shows a more filamentary and compact distribution. At low density, the gas is not efficient at cooling and thus stays hot after its initial impact with the primary star and/or disk material. The hot gas is better able to support a smooth, extended distribution of gas in the disk. At higher density, the gas is able to cool, forming the filamentary structures

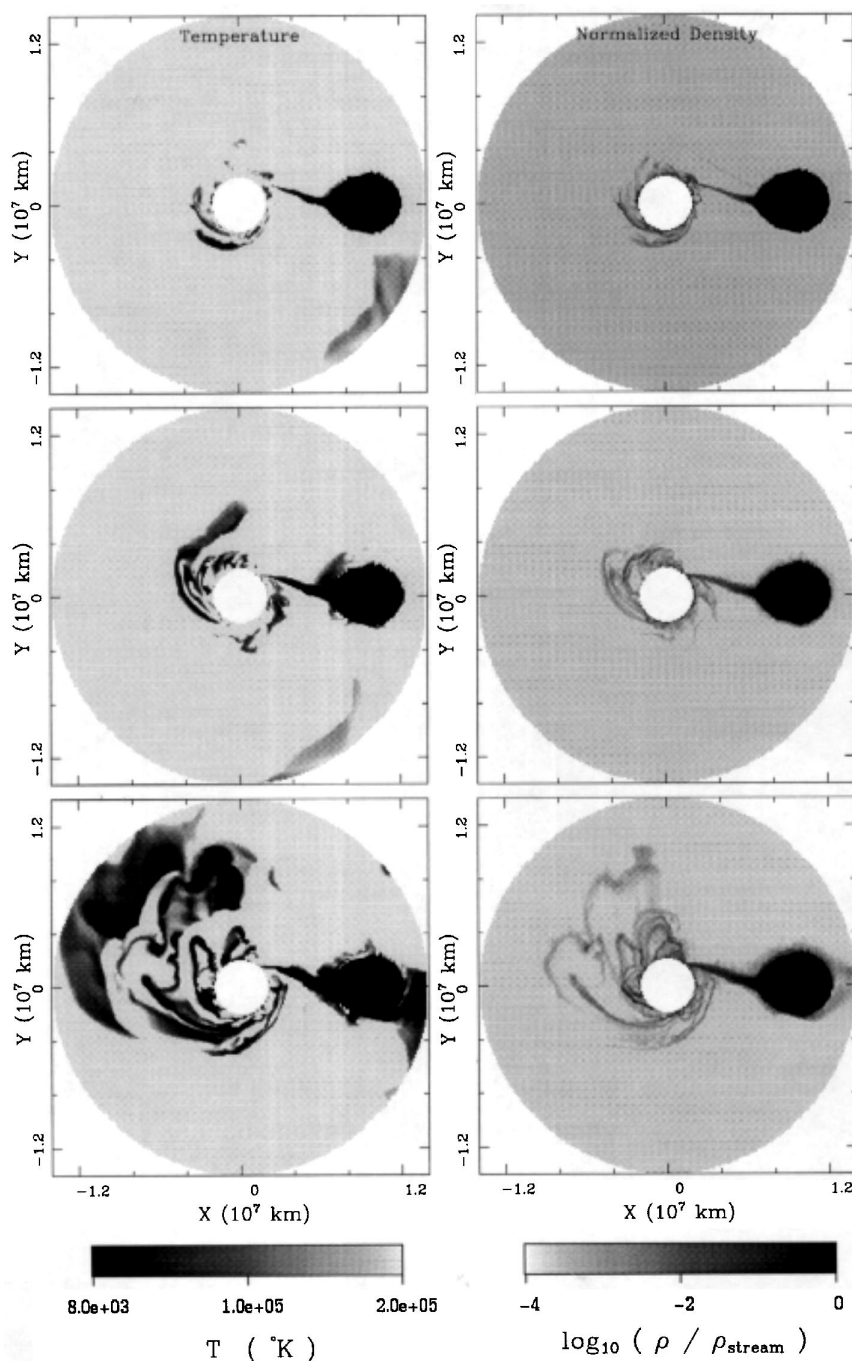


FIG. 7.—Temperature (left-hand column) and density (right-hand column) distribution at time  $t \approx 2.0P_{\text{orb}}$  for the simulations of  $\beta$  Per using three values for the initial gas stream density. From top to bottom, the initial stream densities are  $n_s = 10^8$ ,  $10^9$ , and  $10^{10} \text{ cm}^{-3}$ , respectively. Note that the normalized densities are scaled to the initial stream densities and are displayed using a logarithmic scale.

mentioned previously and collapsing onto the primary star where it is accreted. At the highest density, our inner radial boundary condition is apparently unable to remove a substantial amount of the gas that is being injected into the simulation via the gas stream. For this reason, a large amount of gas piles up around the primary in the simulation. The temperature distribution in each simulation directly reflects the action of the cooling function. The low-density simulation shows the least, while the highest density simulation shows the greatest amount of cool gas. It is also apparent that the dense filaments represent some of the coolest gas in the simulations.

The temperature maps of  $\beta$  Per (see Fig. 7, left-hand column) suggest that the hottest regions are found close to

the location where the gas stream strikes the surface of the mass-gaining star. Here, the temperature reached  $\sim 10^5 \text{ K}$ , where ultraviolet radiation should be detected. The temperature did not reach the  $\sim 10^6 \text{ K}$  suggested by BRM, who predicted that EUV to X-ray emission should be observed.

In addition to looking at emission features only at discrete times during the simulation, the average or overall behavior of this emission was also investigated. As described earlier, 50 individual images at stages in the evolution of the flow from time  $t = P_{\text{orb}}$  to  $2P_{\text{orb}}$  were summed to produce the integrated image. The integrated images obtained from the three simulations of  $\beta$  Per at three differing gas stream densities are shown in Figure 8. This figure also demonstrates the effects of radiative cooling

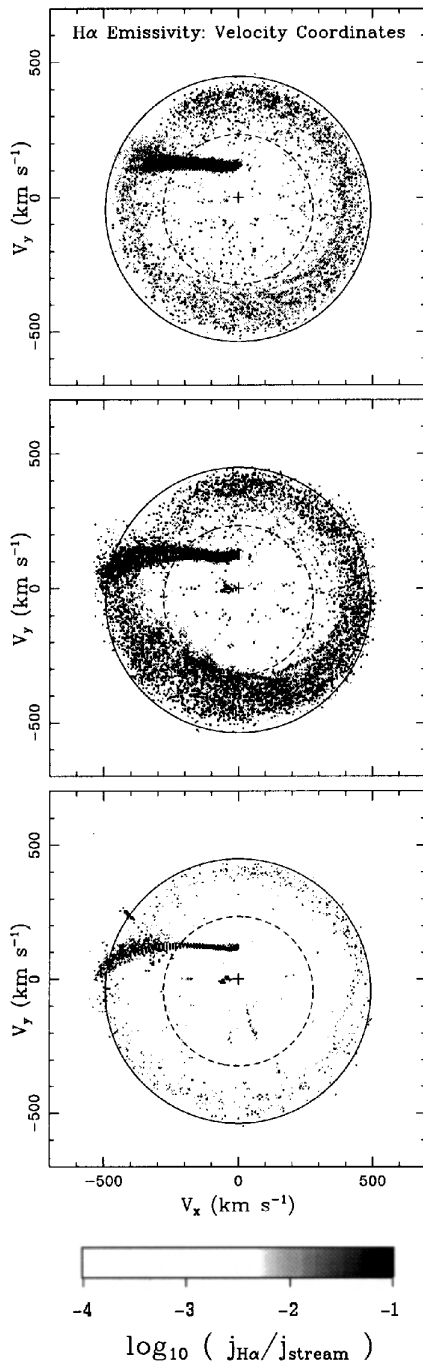


FIG. 8.—Integrated H $\alpha$  emissivity images constructed from the time interval  $1.0P_{\text{orb}} < t < 2.0P_{\text{orb}}$  for the  $\beta$  Per system. The emissivity is scaled to the mean emissivity in the gas stream for each simulation. The initial gas stream density in the simulations was  $n_s = 10^8 \text{ cm}^{-3}$  (top),  $n_s = 10^9 \text{ cm}^{-3}$  (middle), and  $n_s = 10^{10} \text{ cm}^{-3}$  (bottom). See color plate.

on the calculated H $\alpha$  emission. The integrated image for the simulation with initial stream density of  $n_s = 10^9 \text{ cm}^{-3}$  shows that emission from the accretion annulus (between the reference circles) is comparable to that found in the gas stream. On the other hand, the image from the lower density simulation ( $n_s = 10^8 \text{ cm}^{-3}$ ) shows most of this emission to be weaker by a factor of 10 or more than that found in the gas stream. Apparently, the gas in the higher density simulation is able to cool more efficiently to lower temperatures where the H $\alpha$  emissivity of the gas is strongest (Fig. 2). Also, because this cool gas does not have as much

pressure to support itself, it collapses into dense regions about the primary where the H $\alpha$  emissivity is increased further.

The integrated images also show distinct morphologies (Fig. 8). In all three cases, emission from the accretion annulus nearly fills the area between the dashed and solid reference circles, where a Keplerian accretion disk would be located. However, this should not be viewed simply as a classical Keplerian disk. A numerical investigation of the Cartesian and velocity images showed that much of the emission found in the inner regions of the velocity image (low velocities) originates not from the outer radial part of the disk (in spatial coordinates), but from regions very close to the primary star. The average azimuthal velocity of the gas flow close to the primary is relatively slow and chaotic owing to the pressure gradient caused by the impacting stream. Large sections of gas (several grid zones) often showed temporary retrograde motion. This result was not unexpected and illustrated that further examination is usually needed before it can be assumed that these accretion flows take the form of Keplerian accretion disks. These images also demonstrate a lack of symmetry. The part of the ring formed by material at negative  $v_y$  velocities (Fig. 8, lower part of each panel) is generally wider than the parts found at positive velocities (Fig. 8, upper part of each panel). In Figure 8, the annulus is widest at the lower left (negative  $v_y$  and negative  $v_x$ ), where the stream feeds into the circum-primary material, and thinnest in the upper region of the images. The emission from the upper part of the annulus comes mostly from gas in the region between the two stars. Material from the gas stream reaches this region after completing nearly one orbit of the primary. By this time, the gas has dispersed to lower densities by means of internal pressure effects and some material has been accreted by the primary star. Both of these processes reduce the amount of emission expected from gas found in this region and make the corresponding part of the annulus in the upper part of the velocity image fainter.

### 3.2. TT Hya

#### 3.2.1. Parameters Specific to the Binary

The binary system TT Hya consists of an A0 main-sequence primary and a G9 III giant secondary star. The physical parameters of this system appear in Table 1. As with the  $\beta$  Per system, an appropriate choice of stream parameters was required for the simulation.

The temperature of the secondary in this system is similar to that in  $\beta$  Per, so many of the stream parameters were also similar. Since the secondary star from which the stream originates has a low surface temperature, we again set the temperature of the stream at  $T_s = 8000 \text{ K}$ , the minimum temperature allowed in the simulation after considering the effects of the ionizing radiation from the primary star. The adopted sound speed,  $c_s$ , in the stream at the  $L_1$  point was therefore the same as that in  $\beta$  Per. So, once again, the stream was set to leave the  $L_1$  point at  $10 \text{ km s}^{-1}$  in the rotating reference frame of the binary. The diameter of the stream,  $(c_s/\Omega) \approx 8.7 \times 10^{10} \text{ cm}$ , in TT Hya is  $\sim 2.5$  times greater than in  $\beta$  Per (cf. § 3.1.1) because of the longer orbital period of this system. The stream diameter was resolved into three azimuthal zones, as done previously. This required that the grid be divided into 200 azimuthal zones (fewer than in the  $\beta$  Per simulation), whereas 150

zones were used in the radial direction. Observations of the H $\alpha$  emission from this system indicate a mean electron number density in the accretion disk of  $N_e \sim 10^{10} \text{ cm}^{-3}$  (Peters 1989), similar to that in  $\beta$  Per. However, because of the uncertainties in these observations and the cooling time arguments discussed previously for the  $\beta$  Per simulation (see § 3.1.1), we performed three simulations with a range of initial stream densities:  $n_s = 10^8, 10^9$ , and  $10^{10} \text{ cm}^{-3} \text{ s}^{-1}$ .

### 3.2.2. Simulations in Cartesian and Velocity Dimensions

Figure 9 demonstrates the evolution of the flow in TT Hya. The top row of figures shows the system as the gas stream makes a slight grazing impact with the primary. This

impact occurs at approximately  $110^\circ$  from the line of centers as measured from the center of the primary. This behavior is in contrast with  $\beta$  Per, where the gas stream makes a direct impact with the star. Instead, the gas stream in TT Hya has enough room to follow a continuous path around the primary. The high orbital velocity attained during its close approach to the primary causes the still intact gas stream to swing well below the primary in its continuing orbit (Fig. 9, *middle row*). At  $t = 0.25P_{\text{orb}}$ , the gas has completed one orbit of the primary and begins to interact with the gas stream. The gas has followed a very elliptical trajectory owing to the sub-Keplerian velocity with which it originally left the  $L_1$  point. After  $t = 2.0P_{\text{orb}}$  (Fig. 9, *bottom row*), the

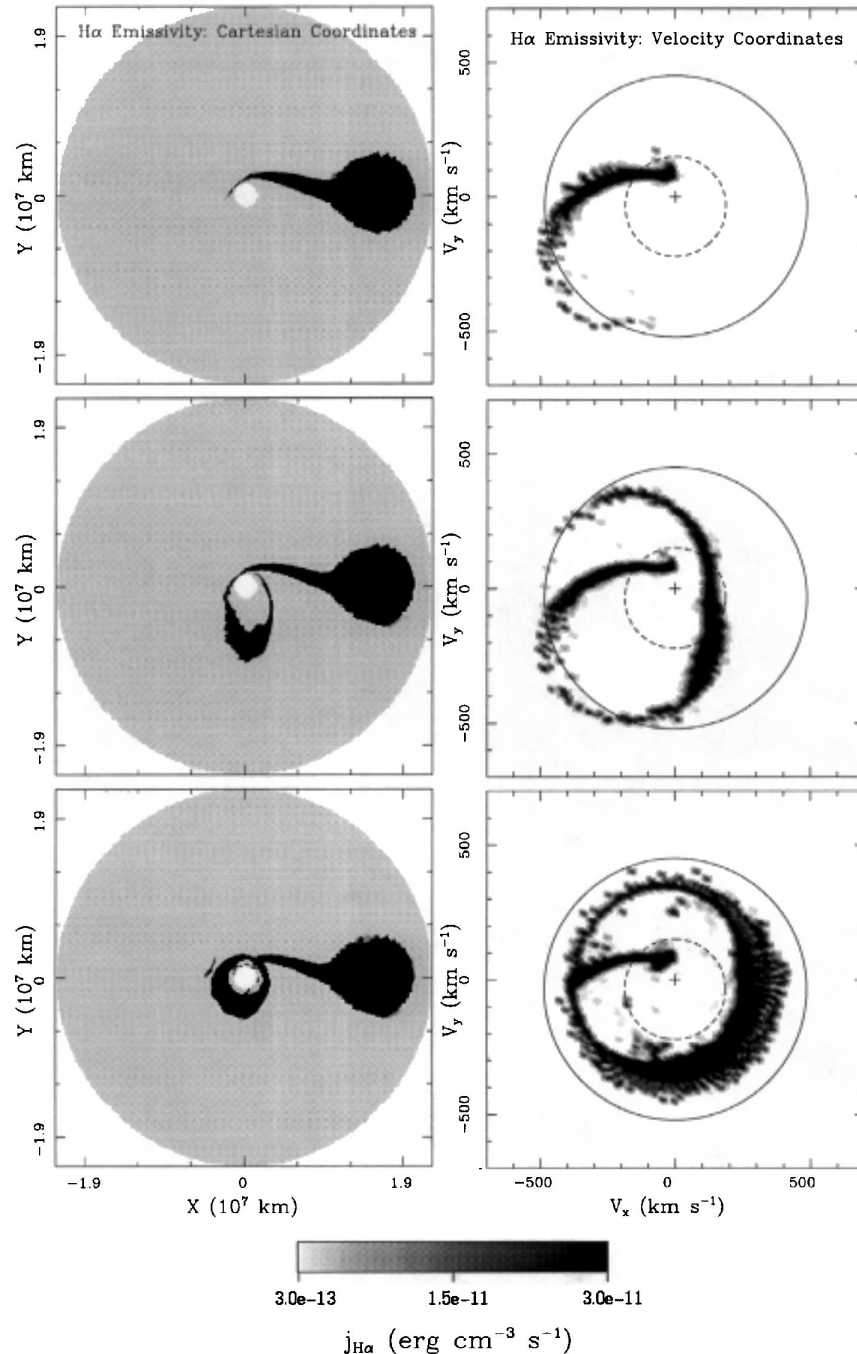


FIG. 9.—Evolution of the H $\alpha$  emissivity of the gas flow in TT Hya. From top to bottom, the images show the system after time  $t = 9.7 \text{ hr} = 0.14P_{\text{orb}}$ ,  $t = 34.7 \text{ hr} = 0.28P_{\text{orb}}$ , and  $t = 68.9 \text{ hr} = 2.0P_{\text{orb}}$ , respectively. The location of H $\alpha$  emission in Cartesian coordinates is shown on the left while the distribution of H $\alpha$  emission in velocity coordinates is shown on the right.

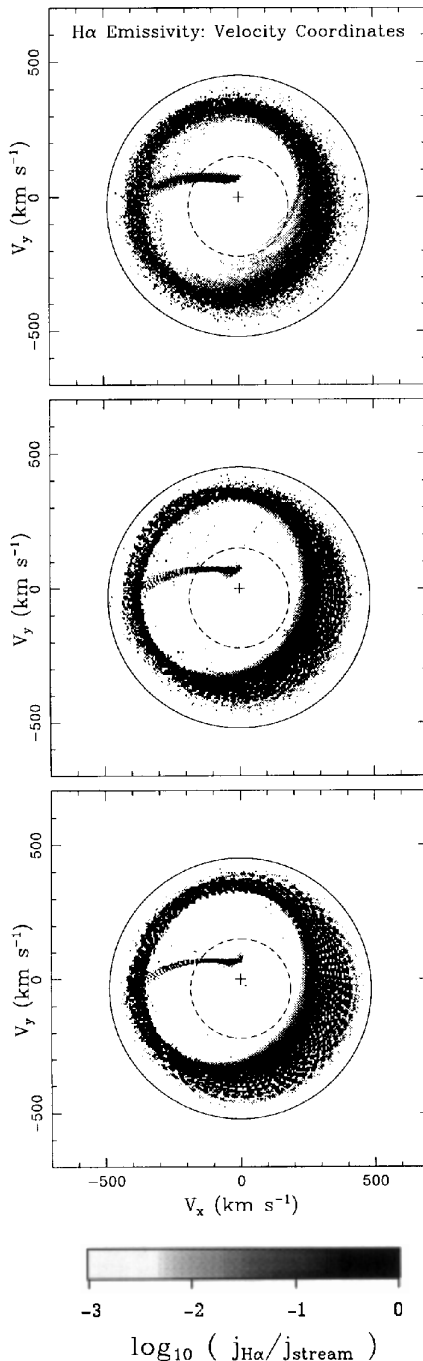


FIG. 10.—Integrated H $\alpha$  emissivity images constructed from the time interval  $1.0P_{\text{orb}} < t < 2.0P_{\text{orb}}$  for the TT Hya system. The emissivity is scaled to the mean emissivity in the gas stream for each simulation. The initial gas stream density in the simulations was  $n_s = 10^8 \text{ cm}^{-3}$  (top),  $n_s = 10^9 \text{ cm}^{-3}$  (middle), and  $n_s = 10^{10} \text{ cm}^{-3}$  (bottom). See color plate.

gas stream simply feeds into a stable, asymmetric accretion annulus. This accretion annulus is elongated toward the lower left in the Cartesian images because of the elliptical trajectories of the gas. Also apparent is the greater radial extent of the accretion annulus toward the lower left of the image and the lesser extent toward the upper right. The direct consequence of this asymmetry in the Cartesian image can be seen in the velocity image where the accretion annulus is generally wider toward the lower right of the image and thinner toward the upper left. This tends to give the illusion that the annulus is off center, when in fact it is

the central hole of the annulus that is off center and not the entire annulus.

The integrated images constructed from the simulations of TT Hya using three different gas stream densities ( $n_s = 10^8, 10^9$ , and  $10^{10} \text{ cm}^{-3}$ ) are all quite similar, especially in morphology (Fig. 10; see also Fig. 11 [Pl. 11] for color version). Since the general shape of the accretion annulus is formed early in the simulation and remains quite stable, all three images (Fig. 10) closely resemble the single velocity image constructed at  $t = 2.0P_{\text{orb}}$  in the simulation described earlier (Fig. 9, bottom row). The integrated images also show the effect of the acceleration of the gas stream as it falls toward the primary. The decrease in density due to the acceleration causes the H $\alpha$  emissivity at the left end of the stream to be a factor of about 10 less than that found in the stream near the  $L_1$  point (right end of the stream). In addition, the ratio of the emissivity found in the accretion annulus to that found in the initial parts of the gas stream increases with the initial gas stream density,  $n_s$  (Fig. 10). This is again caused by the ability of the high-density gas to keep cool and remain dense.

#### 4. DISCUSSION AND CONCLUSIONS

In this section, the results of the hydrodynamic simulations are compared with Doppler tomograms constructed from observational data. The technique of Doppler tomography was first used to obtain images of emission sources in the orbital plane of cataclysmic variables by Marsh & Horne (1988), but there is now an atlas of tomographic images of 18 cataclysmic variables by Kaitchuck et al. (1994). Doppler tomograms of 14 Algol-type binaries including U Sge, U CrB, RS Vul,  $\beta$  Per, SW Cyg, and TT Hya have also been published (e.g., Richards et al. 1995, 1996; Albright & Richards 1996). This technique uses the line profiles obtained at orbital positions around the orbit of the binary to generate a map in velocity coordinates. The main assumption made in this technique is that Doppler broadening dominates thermal and turbulent broadening of the line profiles (Robinson et al. 1993). Synchronous rotation of the components is assumed only to permit the locations of the stars to be plotted on the Doppler map. The tomography calculation does not depend on the assumption that the motion of the gas flows is Keplerian. This latter assumption has been used to convert the Doppler tomograms to Cartesian maps in the case of the cataclysmic variables, but it is not used in the case of the Algols. The technique is easy to use and has been applied to non-astronomical research problems (e.g., in medicine).

The Doppler tomograms constructed from H $\alpha$  emission profiles of  $\beta$  Per (Richards et al. 1996) suggest the presence of a gas stream extending from the  $L_1$  point toward negative  $v_x$  velocities, but there is little evidence of an extended accretion disk surrounding the primary. However, the observational noise level found from observations of  $\beta$  Per can be used to illustrate which accretion flows in the hydrodynamic simulations would be detectable in the observations. Richards et al. (1996) showed that the flux in the gas stream was  $0.1F_c$ , where  $F_c$  is the continuum flux, compared to a  $3\sigma$  significance level of  $0.01F_c$ . Therefore, any emission intensity that is more than a factor of 10 weaker than that found in the gas stream should be hidden in the observational noise. Our hydrodynamic simulations of  $\beta$  Per (Figs. 8 and 11) using the lowest initial stream density,  $n_s = 10^8 \text{ cm}^{-3}$ , show that most of the emission arising from

the accretion annulus is at least a factor of 30 less intense than the brightest parts of the gas stream [i.e.,  $\log(j/j_s) < -1.5$ ]. These features would therefore be undetected in such an observational tomogram of the system. However, our simulation with  $n_s = 10^9 \text{ cm}^{-3}$  shows that the emission from the annulus is more comparable to that found in the stream. So it appears that the initial gas stream density in  $\beta$  Per may be closer to  $10^8 \text{ cm}^{-3}$  than to  $10^9 \text{ cm}^{-3}$ . In this case, the mass transfer in  $\beta$  Per takes place via a low-density gas stream that is unable to cool efficiently from the high temperatures generated by impact with the primary. This high-temperature gas is then unable to produce significant amounts of H $\alpha$  emission except along the gas stream.

In contrast to the  $\beta$  Per system, the 1993 observations of U CrB ( $P_{\text{orb}} = 3.45$  days) and U Sge ( $P_{\text{orb}} = 3.38$  days) show the presence of an accretion annulus in both systems (Albright & Richards 1996). These systems are both quite similar to  $\beta$  Per ( $P_{\text{orb}} = 2.87$  days), since they have similar orbital periods and primary stars with similar spectral types. The dynamics of any mass transfer in these systems is therefore expected to closely resemble that for  $\beta$  Per. The Doppler tomograms of U CrB (1993) and U Sge (1993) show annuli with emission strengths comparable to the strength of emission found along the free-fall path of the gas stream. However, tomograms of these same systems obtained from observations in 1994 (Richards et al. 1995; Albright & Richards 1996) show prominent gas streams with little evidence of accretion annuli. Our hydrodynamic simulations suggest that the changing state of these systems may be due to a change in the density of the gas stream with time; this is an explanation also proposed by Albright & Richards (1996). A dense gas stream would transfer disk material with the ability to cool efficiently after impact with the central star. This gas would have emission strength comparable to that found in the initial parts of the gas stream (1993 observations) than would hotter, less dense gas transferred by a more rarefied gas stream (1994 observations).

The tomogram of TT Hya reveals a toroidal structure similar to the expected shape of a symmetric, Keplerian accretion disk (Albright & Richards 1996). In the Doppler tomogram, a ring of emission was found between the reference circles corresponding to the Keplerian orbital velocity at the surface of the primary and at the  $L_1$  point. This ring appears quite similar to the continuous ring of emission found in the integrated images constructed from our hydrodynamic simulations of TT Hya (Figs. 10 and 11). The ring structures in the tomogram and in the simulated image both show bright emission distributed in a smooth circular pattern about the location of the primary. The tomogram also shows a small patch of emission extending away from the secondary star toward the left-hand side of the image, just above the predicted trajectory of the gas stream. However, since the observations of this system covered an adequate but minimal number of orbital phases, it is difficult to conclude whether this feature is indeed a gas stream similar to the one found in our hydrodynamic simulations. In contrast to our simulated images, the ring of emission in the Doppler tomogram is quite thick and extends inward to velocities less than the Keplerian velocity at the  $L_1$  point (within the inner reference circle). This makes the hole in the ring appear much smaller than the one found in our simulated images. One possible explanation for the smaller hole is that the gas in the TT Hya disk might be hotter than that

found in our simulations. This hot gas would enable the accretion annulus to extend farther out from the primary toward lower orbital velocities. Hot gas would also tend to spread, making a smooth distribution of material about the primary rather than an elliptical structure as seen in the simulations. This could explain why the center of the small hole seen in the tomogram is located near the position of the primary in this system, not off center as in the simulated images (Fig. 10).

The tomograms of cataclysmic variables (CVs) show features similar to those found in the simulations of TT Hya. Since the white dwarf in a CV has a small radius compared to the binary separation, the dynamics of mass transfer are expected to be similar to that found in the long-period Algol binaries. The action of the Coriolis force is sufficient to push the gas stream away from the white dwarf and into an orbit where it can form an accretion disk. Doppler tomograms of the CV systems U Gem and IP Peg (Kaitchuck et al. 1994) show rings of emission with central holes that are somewhat asymmetric. The position of the center of these holes tends to lie left of center (at negative  $v_x$ ) in these images. This off-center location may be indicative of an elongated accretion annulus like that seen in our simulations of TT Hya (Fig. 10).

The temperature structure of the flow was examined in the case of  $\beta$  Per (Fig. 7, *left-hand column*) to provide an additional check on the hydrodynamic model. Our simulations show that the hottest regions are found close to the location where the gas stream strikes the surface of the mass-gaining star. The gas temperature reaches  $\sim 10^5$  K, which is high enough to generate ultraviolet radiation, in agreement with the observations. To date, no X-ray radiation has been detected from the impact region or circumstellar material around the primary. Instead, all X-ray emission is associated with the magnetically active secondary star (see Richards & Albright 1993 and references therein).

The hydrodynamic simulations described here agree quite well with the observed Doppler tomograms. However, further work is needed to improve these simulations. For instance, modeling the surface of the primary star and the accretion process with a partially reflecting boundary condition may oversimplify or ignore important processes that take place during the star-stream interaction. The efficiency with which the photosphere reflects the stream and how gas in the stream and photosphere might mix with one another also needs to be investigated further. In future work we hope to better represent the surface of the primary by modeling a stellar atmosphere in the inner radial zones of the computational grid. Such a model would require better spatial resolution than that used in this work but would produce velocity images much smoother in appearance than those generated in this work. In addition, the question of whether two-dimensional hydrodynamic simulations adequately represent the gas flow in these systems remains to be examined. Three-dimensional simulations of  $\beta$  Per are now in progress (Blondin & Richards 1998) to investigate the distribution of the gas flow in the direction perpendicular to the orbital plane of the binary. This added dimension is expected to reduce the ability of the gas stream to block circumstellar gas from freely orbiting the primary, allowing orbiting gas to flow above and below the gas stream. This effect could change the distribution of gas in both the Cartesian and velocity images, but this does not appear to be

significant at this stage in the research. In addition, the Doppler tomograms of very magnetically active Algols and of the RS CVn binary V711 Tau (HR 1099) display an additional source of emission, namely chromospheric emission, with the same velocity as that of the magnetically active star (Richards & Albright 1995). Therefore, the hydrodynamic simulations described here are correct to first order only because they represent the influence of gravitational forces but not magnetic effects on the gas flows.

In summary, the agreement between the observed and simulated emission features is remarkable. We feel that the results of our simulations capture the most important

dynamical processes in these systems fairly accurately. However, it is clear from the variability of the observed circumstellar emission features in U CrB and U Sge that many epochs of observations will be required before more detailed comparisons can be made with the hydrodynamic simulations.

The authors thank J. Blondin and J. Hawley for their assistance with the VH-1 code, and also thank R. Chevalier, C. Sarazin, D. Whittle and the referee for their comments. This work was partially supported by Air Force Office of Scientific Research grant F49620-94-1-0351 and NASA grant NAG 5-3056 to MTR.

#### REFERENCES

- Albright, G. E., & Richards, M. T. 1996, *ApJL*, 459, 99  
 Birkhoff, G. 1962, *Proc. Symp. Appl. Math.*, 13, 55  
 Blondin, J. M. 1993, *VH-1 Manual*, University of Virginia Technical Report  
 Blondin, J. M., & Richards, M. T. 1998, in preparation  
 Blondin, J. M., Richards, M. T., & Malinkowski, M. L. 1995, *ApJ*, 445, 939  
 Colella, P., & Woodward, P. R. 1984, *J. Comp. Phys.*, 54, 174  
 Cox, D. P., & Daltabuit, E. 1971, *ApJ*, 167, 113  
 Ferland, G. J. 1980, *PASP*, 92, 596  
 Giuricin, G., Mardirossian, F., & Mezzetti, M. 1983, *ApJS*, 52, 35  
 Godunov, S. K. 1959, *Mat. Sb.*, 47, 271  
 Kaitchuck, R. H., Schlegel, E. M., Honeycutt, R. K., Horne, K., Marsh, T. R., White, J. C., & Mansperger, C. S. 1994, *ApJS*, 93, 519  
 Kaitchuck, R. H., Honeycutt, R. K., & Schlegel, E. M. 1985, *PASP*, 97, 1178  
 Kurucz, R. L. 1991, in *Stellar Atmospheres: Beyond Classical Models*, ed. L. Crivellari, I. Hubeny, & D. G. Hummer (Dordrecht: Kluwer), 441  
 Lubow, S. H., & Shu, F. H. 1975, *ApJ*, 198, 383  
 Marsh, T. R., & Horne, K. 1988, *MNRAS*, 235, 269  
 Peters, G. J. 1989, *Space Sci. Rev.*, 50, 9  
 Press, W. H., Flannery, B. P., Teukolsky, S. A., & Vetterling, W. T. 1988, *Numerical Recipes* (Cambridge: Cambridge Univ. Press)  
 Ratliff, M. A. 1996, M.A. thesis, University of Virginia  
 Ratliff, M. A., & Richards, M. T. 1995, *BAAS*, 27, 1343  
 Richards, M. T. 1992, *ApJ*, 387, 329  
 ———. 1993, *ApJS*, 86, 255  
 Richards, M. T., & Albright, G. E. 1993, *ApJS*, 88, 199  
 ———. 1995, in *Stellar Surface Structure*, ed. K. Strassmeier & J. Linsky (Dordrecht: Kluwer), 493  
 Richards, M. T., Albright, G. E., & Bowles, L. M. 1995, *ApJL*, 438, L103  
 Richards, M. T., Jones, R. D., & Swain, M. A. 1996, *ApJ*, 459, 249  
 Robinson, E. L., Marsh, T. R., & Smak, J. I. 1993, in *Accretion Disks in Compact Stellar Systems*, ed. J. C. Wheeler (Singapore: World Scientific), 75  
 Russ, J. C. 1992, *The Image Processing Handbook* (Ann Arbor: CRC Press)  
 Shore, S. N. 1992, *An Introduction to Astrophysical Hydrodynamics* (San Diego: Academic Press)  
 Sutherland, R. S., & Dopita, M. A. 1993, *ApJS*, 88, 253  
 Tritton, D. J. 1988, *Physical Fluid Dynamics* (Oxford: Oxford Univ. Press)  
 Ulrich, R. K., & Burger, H. L. 1976, *ApJ*, 206, 509  
 Vesper, D., & Honeycutt, R. K. 1993, *PASP*, 105, 731  
 Wu, K., Chanmugan, G., & Shaviv, G. 1994, *ApJ*, 426, 664



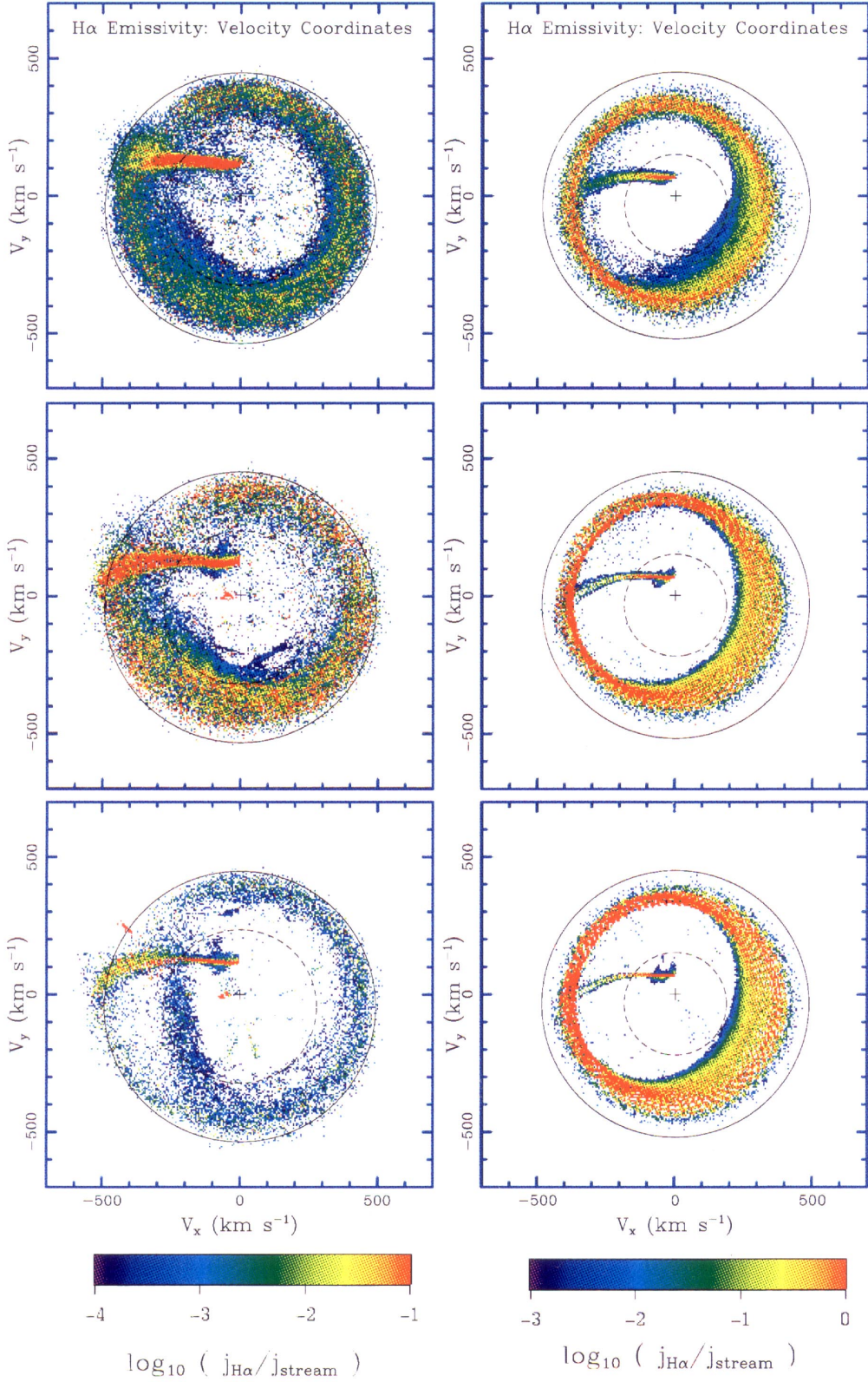


FIG. 11.—A color version of Figs. 8 and 10 combined, which shows the integrated H $\alpha$  emissivity images constructed from the time interval  $1.0P_{\text{orb}} < t < 2.0P_{\text{orb}}$  for  $\beta$  Per (left-hand column) and TT Hya (right-hand column). The emissivity is scaled to the mean emissivity in the gas stream for each simulation. The initial gas stream density in the simulations was  $n_s = 10^8 \text{ cm}^{-3}$  (top row),  $n_s = 10^9 \text{ cm}^{-3}$  (middle row), and  $n_s = 10^{10} \text{ cm}^{-3}$  (bottom row).

RICHARDS & RATLIFF (see 493, 339)